Available online at www.sciencedirect.com
SCIENCE DIRECT®
Journal of Solid State Chemistry 178 (2005) 2133–2143
JOURNAL OF SOLID STATE CHEMISTRY
www.elsevier.com/locate/jssc

Where are the Sn atoms in $LaSb_2Sn_x$, $0.1 \leqslant x \leqslant \sim 0.75$?

Lasse Norén, Ray L. Withers*, Frank J. Brink

Research School of Chemistry, Australian National University, Canberra, ACT 0200, Australia

Received 22 March 2005; received in revised form 20 April 2005; accepted 24 April 2005

Abstract

The composition range and (composite modulated) structure of compounds within the wide range non-stoichiometric $LaSb_2Sn_x$, $0.1 \leqslant x \leqslant 0.75$, solid solution is carefully investigated via a combined electron diffraction, XRD and electron probe microanalysis study. Evidence for metastability of the $LaSb_2Sn_x$ phase at the low x composition end of the solid solution is presented. Direct evidence is found for a reasonably (although by no means perfectly) well ordered Sn sub-structure which is, in general, mutually incommensurable with respect to a very well ordered underlying $LaSb_2$ sub-structure along both a and c directions. The overall $(3+2)$-d superspace group symmetry is given along with a discussion of the consequences as regards the arrangement of the Sn atoms. The Sn sub-structure c-axis cell dimension shows very little variation with composition x providing direct experimental evidence of the importance of Sn–Sn metallic bonding (along one-dimensional [001] Sn strings) for the stability of the phase.

Keywords: $LaSb_2Sn_x$; Composite modulated structure; Sn–Sn metallic bonding; Wide range non-stoichiometric solid solution

1. Introduction

An extensive new family of wide range non-stoichiometric, layered rare earth tin antimonides $LnSb_2Sn_x$, $0.1 \leqslant x \leqslant \sim 0.75$, ($Ln$ = La, Ce, Pr, Nd and Sm) has only relatively recently been reported [1,2]. The existence of this family of materials, and in particular, their apparently widely variable Sn content, raises intriguing questions as to what the appropriate electron counting rules and the role of Sn atoms in the structure might be [1–4]. The *Cmcm* average structures, for $x = 0.5$ and 0.75 [1,2], have now been reported (see Fig. 1a). They are built out of $(LaSb_2)_2$ bi-layers perpendicular to **b** (shaded in Fig. 1a) separated by one-dimensional oscillating strings of (apparently) partially occupied Sn atom sites running along the c-direction (see Fig. 1a).

The $(LaSb_2)_2$ (in general $(MAB)_2$) bi-layer unit is a common structural element in many binary f-element pnictides or chalcogenides (such as e.g. $SmSb_2$ [5]—see Fig. 1b) as well as ternary combinations thereof (such as e.g. ThAsSe [6,7]—see Fig. 1c). It is formed by an –A–M–B–M–A– consecutive layer stacking of A (a pnictide or chalcogenide), M (a metal) and B (a pnictide or chalcogenide) square nets along the (long) b-axis direction (as defined in Fig. 1a)—in the case of $LaSb_2Sn_x$, with an –Sb(2)–La–Sb(1)–La–Sb(2)– stacking sequence [1,2] (see Fig. 1a). One such Sb(2)–La–Sb(1) sequence gives rise to a single layer of face-sharing MA_4B_4 "square antiprisms" (a somewhat erroneous term as the edges of the square A(Sb(2))-face are $\sqrt{2}$ larger than those of the B(Sb(1))-face [1,2]). Two consecutive layers of such MA_4B_4 antiprisms are then connected through the intermediate Sb(1) atoms (forming the B-face) via edge sharing to form the bi-layer itself (see Fig. 1a).

Inserted between these $(LaSb_2)_2$ bi-layer units are Sn atoms forming one-dimensional oscillating strings along the c-direction (see Fig. 1a). Whilst the atoms comprising the $(LaSb_2)_2$ bi-layers and the overall $LaSb_2$ sub-structure itself are fully occupied and crystallographically well defined [1,2], the local arrangement of the Sn atoms is most definitely not [1,2]. The Sn atoms are, for example, reported to occupy three crystallographically

*Corresponding author. Fax: +61 2 6125 0750.
E-mail address: withers@rsc.anu.edu.au (R.L. Withers).

0022-4596/$ - see front matter © 2005 Elsevier Inc. All rights reserved.
doi:10.1016/j.jssc.2005.04.026

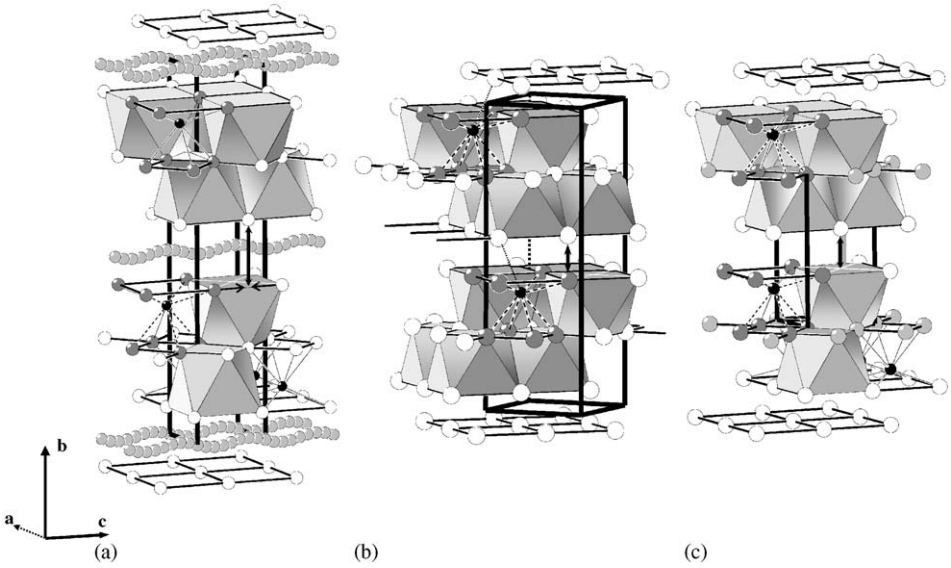

Fig. 1. The reported average structure of (a) $LaSb_2Sn_{0.75}$ along with the closely related structures of (b) $LaSb_2$ and (c) ThAsSe are shown. See text for details.

independent, partially occupied sites (at the ~19% level in the case of the maximal Sn content, $x = 0.75$ compound [1] and at about the ~13% level in the case of the $x = 0.5$ compound [2]) whilst the separation distance between the nearest neighbour such Sn sites is only ~0.5–0.6 Å, far too close together to be simultaneously occupied [1,2] (see e.g. Fig. 3 of [2]). Clearly, the reported crystal structures [1,2] are only average structures, at least as far as the tin atoms are concerned.

Given these reported crystal structures, the closest possible Sn–Sn separation distance within any one [001] string (and the only one that would correspond to a reasonable Sn–Sn bonding distance [2]) is ~2.8 Å and corresponds to fully occupying every fifth potential Sn site along each [001] string (see Fig. 3 of [2]). Such a one-dimensionally ordered arrangement of Sn atoms along each [001] string would give rise to an overall Sn content of $x = 0.8$, close to the reported maximal Sn content, x~0.75 compound. Whether such an arrangement would be correlated from one such [001] string to the next and in what manner, however, is not apparent. Likewise, when the overall Sn content is reduced from $x = 0.8$, it is not so clear what the local arrangement of Sn atoms should be along any one particular [001] string direction (see Fig. 3 of [2]). Nonetheless, one might expect at least some diffraction evidence for local ordering (either in the form of additional satellite reflections, see e.g. [8]—or perhaps, for example, structured diffuse scattering—see e.g. [9]) accompanying the strong Bragg reflections of the underlying $LaSb_2$ sub-structure.

To date, however, no evidence for any such local ordering of the Sn atoms has been found [1,2]. Given the proven ability of electron diffraction to reveal weak features of reciprocal space missed by more conventional powder diffraction techniques, the purpose of the current paper is to present the results of a careful electron diffraction investigation of the reciprocal space of this wide range non-stoichiometric $LaSb_2Sn_x$ solid solution looking in particular for diffraction evidence of Sn ordering and associated structural relaxation.

2. Experimental

2.1. Synthesis

The $x = 0.3$, 0.5 and 0.6 members of the reported $LaSb_2Sn_x$, $0.1 \leqslant x \leqslant$ ~0.75, solid solution were initially synthesized following the method used by Ferguson et al. [1] i.e. by reacting stoichiometric amounts of the pure elements in evacuated silica tubes, first heat treated at 570 °C overnight and then at 950 °C for a further 2 days followed by a slow cooling to room temperature over 24 h. The XRD patterns of all $LaSb_2Sn_x$ compounds synthesized in this manner initially appeared single phase and could indeed be indexed to an orthorhombic *Cmcm* unit cell with lattice parameters quite close to those reported in [1].

In the case of the $x = 0.5$ compound, however, there were at least two weak to medium strength additional lines which could not be indexed on the *Cmcm* unit cell. In the case of the $x = 0.3$ compound, these same lines were again present (although weaker) as well as a further six or seven other additional lines (two of which were relatively strong) which also could not be indexed to the *Cmcm* unit cell. In the case of the $x = 0.6$ compound, these additional lines were not present. It was thus

Table 1
Refined unit cell parameters for the various $LaSb_2Sn_x$ compounds

No.	x	Reaction time and temp.	a	b	c
1a*	0.3	2 d (950 °C)	4.2622(3)	23.1305(14)	4.4799(3)
1b*	0.3	+ 19 d (500 °C)	4.2617(3)	23.1362(14)	4.4854(3)
1c*	0.3	+ 19 d (850 °C)	Decomposed		
2a*	0.5	2 d (950 °C)	4.2611(3)	23.1334(14)	4.4863(3)
2b	0.5	+ 30 d (850 °C)	4.2579(4)	23.1503(13)	4.4992(6)
3a	0.6	2 d (950 °C)	4.2569(4)	23.1495(22)	4.4985(6)
3b	0.6	+ 24 d (500 °C) + 17 d (600 °C)	4.2609(3)	23.1452(14)	4.4916(4)

The compositions, x, are given "as made", the reaction time in days (d), the reaction temperature in degrees Celsius and the refined cell parameters in ångström (Å). Multi-phase samples indicated with an *.

unclear whether or not equilibrium had been reached, particularly for the lower x compounds.

The remaining materials were thus ground, pressed into pellets and re-annealed for further periods of time at 500, 600 and/or 850 °C. This treatment was continued until no further changes in the unit cell parameters of the $LaSb_2Sn_x$ phase or otherwise could be detected via X-ray powder diffraction (XRD), at which point the reaction was assumed to have reached equilibrium.

2.2. X-ray diffraction

The XRD patterns were collected using a Guinier-Hägg camera with Cu $K_{\alpha 1}$ radiation. Silicon (NBS No. 640) was used as an internal standard to accurately determine unit cell parameters, refined using the "Unitcell" software package [10].

2.3. Electron probe microanalysis

Electron probe microanalysis (EPMA) was performed to check homogeneity and to verify the compositions of the synthesized compounds. The samples were prepared by mounting in resin followed by polishing to $<1\,\mu m$. The analyses were carried out on a JEOL 6400 scanning electron microscope (SEM) equipped with an Oxford light element EDS detector and Link ISIS SEMquant software using the settings 15 kV and 1 nA. In order to minimize the atomic number, absorption and fluorescence (ZAF) corrections, stoichiometric SnSb was used as a calibration standard to determine the Sn/Sb ratio while the $LaSb_2Sn_{0.6}$ compound was used as a calibration standard to determine La/Sb ratios for the non-$LaSb_2Sn_x$ phases.

2.4. Electron diffraction

Transmission electron microscope (TEM) analysis was carried out on a Philips EM 430 TEM on crushed grains of the samples dispersed onto holey carbon-coated copper grids.

3. Results

3.1. X-ray diffraction and EDS analysis

The X-ray powder patterns of the initially synthesized (2 days at 950 °C) $LaSb_2Sn_x$ compounds appeared single phase on first inspection (as mentioned above) and could be indexed to an orthorhombic *Cmcm* unit cell with lattice parameters as given in Table 1. On closer inspection and using longer exposure times, however, medium strength additional lines were clearly present in the case of the $x = 0.3$ and 0.5 compounds (particularly the $x = 0.3$ compound) which could not be indexed to this *Cmcm* unit cell. By contrast, no additional lines were present in either the initially synthesized, or the longer term annealed, $LaSb_2Sn_{0.6}$ compound. EPMA analysis confirmed the homogeneity of these latter $LaSb_2Sn_{0.6}$ samples as well as the overall composition ($LaSb_2Sn_{0.60(3)}$—6 separate analyses). In each case, the refined unit cell parameters of these $LaSb_2Sn_x$ compounds were found to change slightly upon further annealing, suggesting that the initial 2 days annealing at 950 °C is insufficient to reach equilibrium.

Prolonged heat treatment at 850 °C in the case of the $x = 0.5$ compound led to the systematic disappearance of the two initially observed, weak to medium strength additional lines leaving only the lines of the single-phase $LaSb_2Sn_{0.5}$ compound. The refined lattice parameters of this $LaSb_2Sn_{0.5}$ phase showed a small but systematic decrease in a and increase in b and c with longer term annealing (see Table 1).

To investigate the stability of the initially multi-phase $x = 0.3$ compound, a sample with the nominal composition $LaSb_2Sn_{0.3}$ was separated into three batches which were then given different heat-treatments. The first batch was kept as synthesized according to Ferguson et al. [1] while the second and third batches were pressed into pellets and heat treated at 500 and 850 °C, respectively, for periods up to 19 days. The resultant samples were then investigated using XRD and EPMA. Prolonged heat treatment at 500 °C in the case of the $x = 0.3$ sample led to some changes in relative intensities but did not remove the additional lines, i.e. the sample

remained multi-phase. The refined lattice parameters of the $LaSb_2Sn_x$ phase in the sample again showed a small decrease in a and increase in b and c with increased annealing time.

Heat treatment at 850 °C for 19 days led to the decomposition, and hence disappearance of the lines, of the $LaSb_2Sn_x$ compound. The sample showed a brownish coating on the inside of the tube walls while the pressed pellets showed metallic-like droplets forming in the grain boundary regions of the pellet. EPMA analysis (5 separate analyses) gave the average bulk composition of this "drop-like" phase as $La_{0.03(4)}Sn_{0.42(11)}Sb_{0.55(9)}$ but with significant variation from drop to drop as reflected in the estimated error bars. The composition of the pellet itself was much more uniform with an average bulk composition (5 separate analyses) of $La_{0.352(2)}Sb_{0.640(3)}Sn_{0.009(3)}$, i.e. relatively close to the composition $LaSb_2$ [5].

The powder diffraction pattern of this phase, however, was not indexable on the cell reported for $LaSb_2$ [5] or on any of the other cells reported for phases in this system. (Unfortunately, too few lines were observed to attempt to fit to a trial unit cell.) The strongest lines of the phase account for the majority (as well as the strongest) of the additional lines detected in the initially synthesized $x = 0.3$ compound. This suggests that the nominal $LaSb_2Sn_{0.3}$ composition is in a two-phase, or possibly even three-phase, region of the ternary phase diagram and thus phase separates into at least a Sn-poor phase (with composition close to $La_{0.352(2)}Sb_{0.640(3)}Sn_{0.009(3)}$) and a Sn-rich $LaSb_2Sn_x$ compound with x significantly >0.3. EPMA analysis of the $x = 0.3$ samples indeed show both tin-rich (with composition $LaSb_2Sn_{0.45(2)}$) and tin-poor ($La_{1.10(2)}Sb_{2.00(3)}Sn_{0.04(4)}$) regions with respect to the nominal $LaSb_2Sn_{0.3}$ composition. Fig. 2, for example, shows (a) an electron back-scattered image and (b) La, (c) Sb and (d) Sn X-ray intensity maps respectively taken from the same region of a typical grain of the initially synthesized $x = 0.3$ sample. The Sn-rich and Sn-poor regions are clearly apparent in the Sn X-ray intensity map of this grain (see Fig. 2d).

Taken in total, the above results indicate that the $LaSb_2Sn_x$ solid solution (for low x) may only be metastable and that the equilibrium lower composition bound for the $LaSb_2Sn_x$ solid solution is more like ~0.45 than 0.1. Nonetheless, the $LaSb_2Sn_x$ solid solution still exists over an extensive composition range, $\sim 0.45 \leqslant x \leqslant \sim 0.75$. In the remainder of this paper, we focus on the crystallography and crystal chemistry of this solid solution phase.

3.2. Electron diffraction

Fig. 3 shows (a) and (b) $[010]_p$, (c) $[01\bar{1}]_p$ and (d) $[\bar{2}10]_p$ zone axis electron diffraction patterns (EDPs) typical of the long-term annealed $LaSb_2Sn_x$ compounds indexed with respect to the reported *Cmcm* average structure unit cell [1,2] (in conventional three index notation with the subscript p). EDPs at the same zone axis orientation show some, but remarkably little, variation with Sn content x (cf., for example, the $[010]_p$ zone axis EDP of Fig. 3a with that of Fig. 3b, etc.). Fig. 3a is from the $x = 0.5$ compound, Fig. 3b from the nominally $x = 0.3$ compound (x~0.45 from EPMA) and Figs. 3c and d from the $x = 0.6$ compound. Note that the extinction conditions associated with the strong, sharp Bragg reflections of the underlying $LaSb_2$ sub-structure ($F(hkl) = 0$ unless $h+k$ even and $F(h0l) = 0$ unless h and l are both even) are consistent with the *Cmcm* average structure space group symmetry reported for these compounds [1,2].

Accompanying these strong, sharp $LaSb_2$ sub-structure Bragg reflections (henceforth labelled **G**) are a set of (in general) incommensurate (along both $\mathbf{a}_p^*$ and $\mathbf{c}_p^*$) satellite reflections, occurring very close to the $\mathbf{G} \pm \frac{1}{4}[202]_p^*$ and $\mathbf{G} \pm \frac{1}{4}[20\bar{2}]_p^*$ regions of reciprocal space in Figs. 3a,b,d and to the $\mathbf{G} \pm \frac{1}{2}[111]_p^*$ and $\mathbf{G} \pm \frac{1}{2}[1\bar{1}\bar{1}]_p^*$ regions of reciprocal space in Fig. 3c. Note also that these additional satellite reflections, while they appear relatively sharp, are nonetheless accompanied by diffuse streaking perpendicular to the $\mathbf{c}_p^*$ direction of reciprocal space in each of the EDP's shown in Fig. 3. Note further that the $\mathbf{G} \pm \sim\frac{1}{4}[202]_p^* = \mathbf{G} \pm \sim\frac{1}{2}[101]_p^*$ satellite reflections (in Figs. 3a, b and d) are actually quite close in reciprocal space to the $\mathbf{G} \pm \sim\frac{1}{2}[111]_p^*$ regions of reciprocal space (in Fig. 3c) when the rather long b~23.1 Å axis of these materials as well as the possible existence of diffuse streaking along $\mathbf{b}_p^*$ is taken into account.

The existence of diffuse streaking running through these same satellite reflections along $\mathbf{b}_p^*$ is confirmed by the typical (a) $[\bar{1}01]_p$, (b) $[102]_p$, (c) $[\bar{1}03]_p$ and (d) $[001]_p$ zone axis EDPs of these $LaSn_xSb_2$ compounds shown in Fig. 4. This time Figs. 4a and d are from the $x = 0.5$ compound while Figs. 4b and c are from the $x = 0.6$ compound. Again, EDPs from the same zone axis orientation are always very similar regardless of composition. Indexation with the subscript p is again with respect to the underlying *Cmcm*, $LaSb_2$, average sub-structure. Note the existence of considerable diffuse streaking along the $\mathbf{b}_p^*$ direction running through the $\mathbf{G} \pm \sim\frac{1}{4}[202]_p^*$ satellite reflections in (a) and (c) as well as the absence of satellite reflections at the $\mathbf{G} \pm \sim\frac{1}{2}[111]_p^*$ regions of reciprocal space in Fig. 4a. This confirms that incommensurate 'satellite reflections' do indeed only occur at the $\mathbf{G} \pm \sim\frac{1}{4}[202]_p^*$ and $\mathbf{G} \pm \sim\frac{1}{4}[20\bar{2}]_p^*$ (as well as higher order linear combinations thereof) regions of reciprocal space and that the apparent presence of $\mathbf{G} \pm \frac{1}{2}[111]_p^*$ satellite reflections in Fig. 3c arises from diffuse streaking running through the $\mathbf{G} \pm \sim\frac{1}{4}[202]_p^*$ satellite reflections along the very short $\mathbf{b}_p^*$ direction.

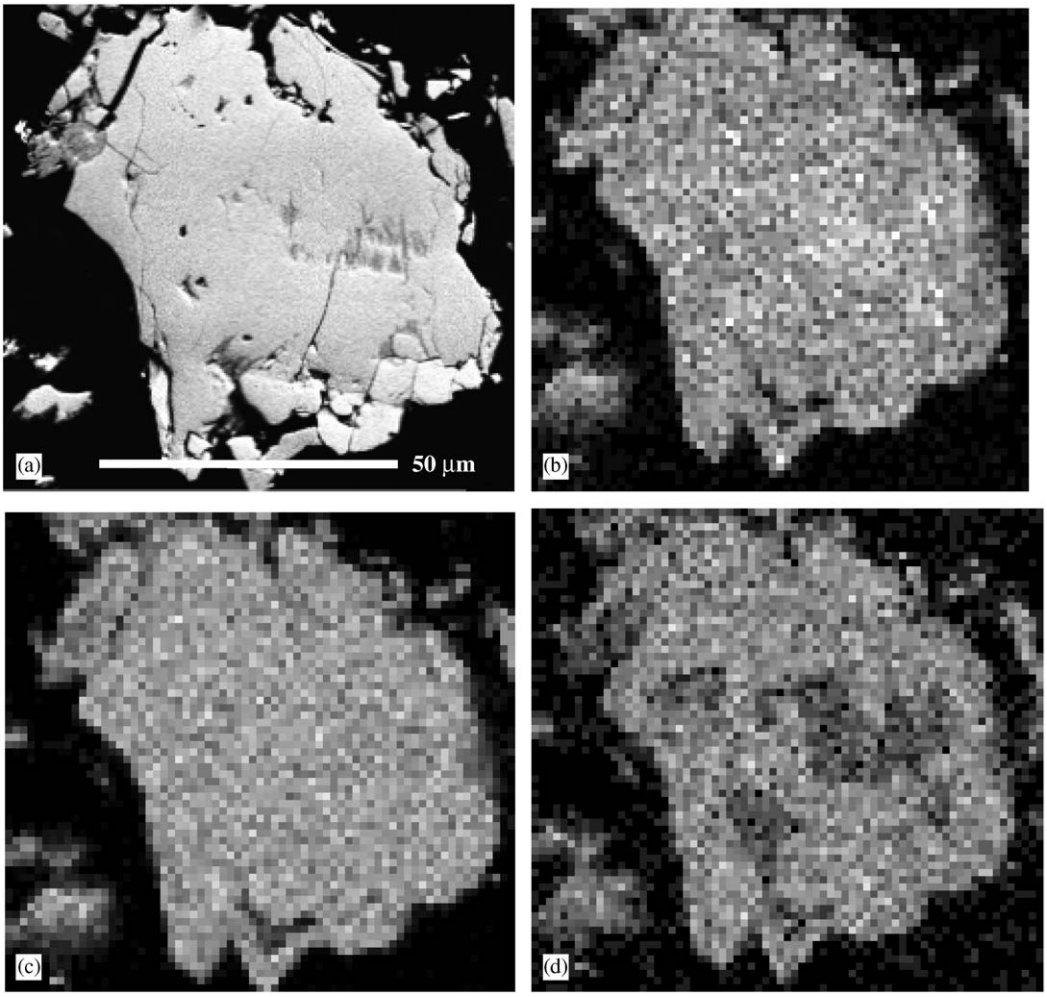

Fig. 2. (a) An electron back-scattered image of a typical grain of the initially synthesized $x = 0.3$ sample along with (b) La, (c) Sb and (d) Sn X-ray intensity maps from the same region.

Returning to the $[010]_p$ zone axis EDPs of Figs. 3a and b, it is clear that integer indexation of these, in general, $(3+2)$-d incommensurately modulated structure/s [8,11] must be with respect to five basis vectors which can be chosen to be $M* = \{\mathbf{a}_p^*, \mathbf{b}_p^*, \mathbf{c}_p^*, \mathbf{q}_1 = (\frac{1}{2} + \varepsilon_1)\mathbf{a}_p^*$ and $\mathbf{q}_2 = 2\mathbf{c}_p^* - (\frac{1}{2} + \varepsilon^2)\mathbf{c}_p^* = (\frac{3}{2} - \varepsilon^2)\mathbf{c}_p^*\}$. The parameters ε_1 and ε_2, while always small, are in general positive and non-zero (see e.g. Fig. 3a) (except in the case of the nominally $x = 0.3$ compound where ε_1 appears to be zero (see e.g. Fig. 3b)). The five integer indexation in Figs. 3 and 4 is thus with respect to this basis vector set.

It might reasonably be asked why $\mathbf{q}_2$ is not simply chosen to be $(\frac{1}{2} + \varepsilon_2)\mathbf{c}_p^*$ rather than $(\frac{3}{2} - \varepsilon_2)\mathbf{c}_p^*$ as chosen above. For a conventional incommensurately modulated structure, this would represent a rather simpler indexation scheme. The reason that it is not the most appropriate in the current case is suggested by, for example, the $[010]_p$ convergent beam EDP shown in Fig. 5a—in particular, by the obvious disparity in relative intensities between the strongest satellite reflections immediately on either side of parent $LaSb_2$ sub-structure reflections such as, for example, that labelled 0 0 2 0 0. (Note also the general weakness of the satellite reflections relative to the strong Bragg reflections of the $LaSb_2$ sub-structure. This explains the dominance of the $LaSb_2$ sub-structure Bragg reflections in the X-ray powder data.) The satellite reflections on the low-angle side (labelled 0 0 0 1 1 and 0 0 0 $\bar{1}$ 1 in Fig. 5a) are significantly more intense than the equivalent satellite reflections on the high-angle side (labelled 0 0 4 1 $\bar{1}$ and 0 0 4 $\bar{1}$ $\bar{1}$ in Fig. 5a). This is not compatible with a conventional incommensurately modulated structure [12].

It suggests instead a composite modulated structure interpretation [8,11,12] whereby the reflection labelled 0 0 2 0 0 in Fig. 5 corresponds to a parent [002]* Bragg reflection of one component sub-structure (the $LaSb_2$ sub-structure) while the reflections labelled 0 0 0 1 1 and 0 0 0 $\bar{1}$ 1 in Fig. 5 correspond to parent Bragg reflections

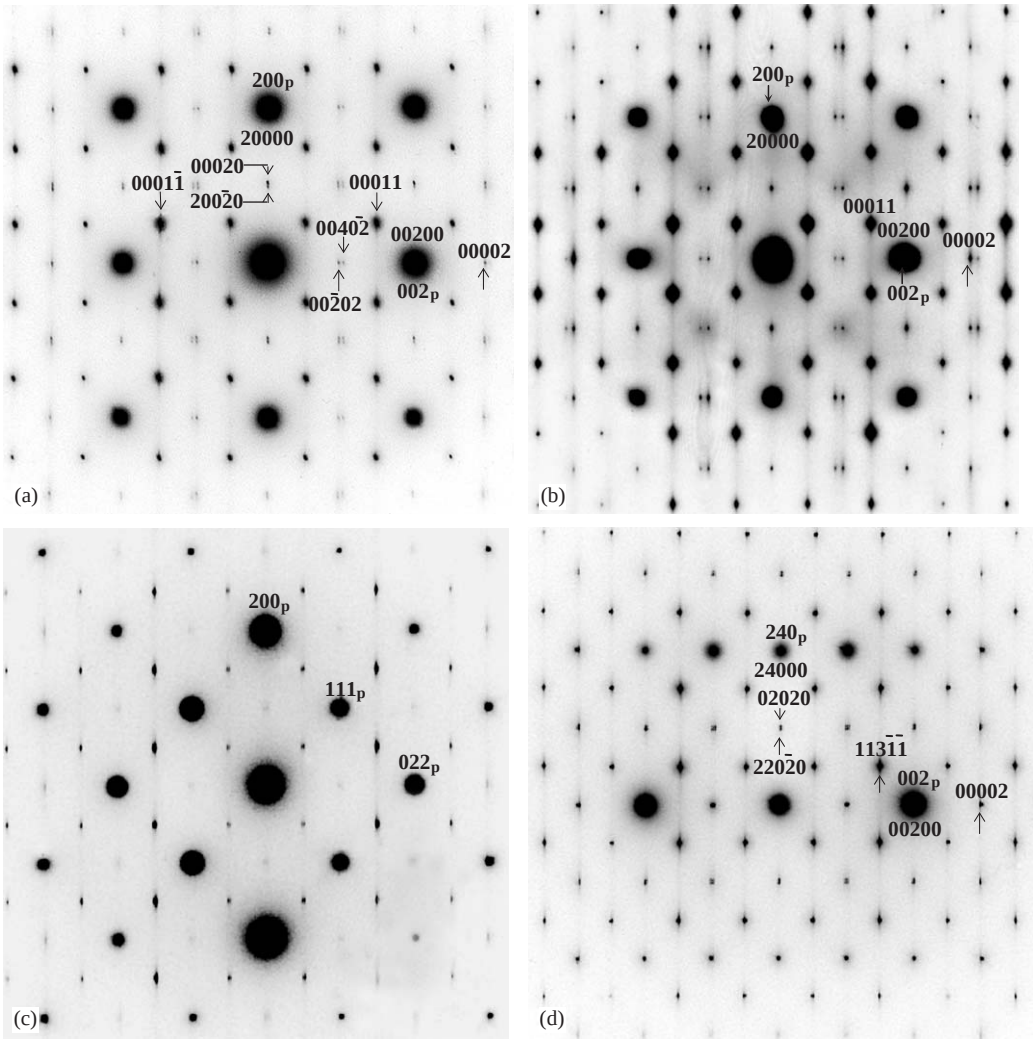

Fig. 3. (a) and (b) $[010]_p$, (c) $[01\bar{1}]_p$ and (d) $[\bar{2}10]_p$ zone axis electron diffraction patterns (EDP's) typical of the long-term annealed $LaSb_2Sn_x$ compounds indexed with respect to the reported *Cmcm* average structure unit cell (in conventional three index notation with the subscript p, in five index notation see the text). (a) Is from the $x = 0.5$ compound, (b) from the nominally $x = 0.3$ compound (x~0.45 from EPMA) and (c) and (d) from the $x = 0.6$ compound.

(in this case [101]* and $[\bar{1}01]$*) of a second component sub-structure (the Sn sub-structure) i.e. the five basis vectors chosen earlier to index the EDPs shown in Figs. 3–5 are given by

$$M* = \{\mathbf{a}_p^* = \mathbf{a}_{LaSb2}^*, \mathbf{b}_p^* = \mathbf{b}_{LaSb2}^* = \mathbf{b}_{Sn}^*,$$
$$\mathbf{c}_p^* = \mathbf{c}_{LaSb2}^*, \mathbf{q}_1 = (\tfrac{1}{2} + \varepsilon_1)\mathbf{a}_p^* = (\tfrac{1}{2} + \varepsilon_1)\mathbf{a}_{LaSb2}^* = \mathbf{a}_{Sn}^* \text{ and}$$
$$\mathbf{q}_2 = (\tfrac{3}{2} - \varepsilon_2)\mathbf{c}_p^* = (\tfrac{3}{2} - \varepsilon_2)\mathbf{c}_{LaSb2}^* = \mathbf{c}_{Sn}^*\}.$$

The validity of this (composite modulated structure) interpretation is confirmed by the close to $[010]_p$ EDP of the (initially synthesized) nominally $x = 0.3$ compound shown in Fig. 5b. This EDP was obtained by tilting a few degrees away from an exact $[010]_p$ zone axis orientation (such as that shown in Fig. 5a) around a 200_p* systematic row (see e.g. Figs. 3a,b). Such tilting dramatically diminishes the dynamical intensity redistribution of the parent Sn sub-structure Bragg reflections arising from multiple scattering by the $LaSb_2$ sub-structure Bragg reflections and shows clearly that the strongest of the additional 'satellite' reflections indeed correspond to the parent reflections of the Sn sub-structure as defined above.

The so-called W matrix [8,11] which transforms the above set of basis vectors into that appropriate for the Sn sub-structure i.e $M_{Sn}* = \{\mathbf{a}_{Sn}*, \mathbf{b}_{Sn}*, \mathbf{c}_{Sn}*, \mathbf{a}_{LaSb2}*, \mathbf{c}_{LaSb2}*\}$ is then given by

$$W = \begin{pmatrix} 0 & 0 & 0 & 1 & 0 \\ 0 & 1 & 0 & 0 & 0 \\ 0 & 0 & 0 & 0 & 1 \\ 1 & 0 & 0 & 0 & 0 \\ 0 & 0 & 1 & 0 & 0 \end{pmatrix}.$$

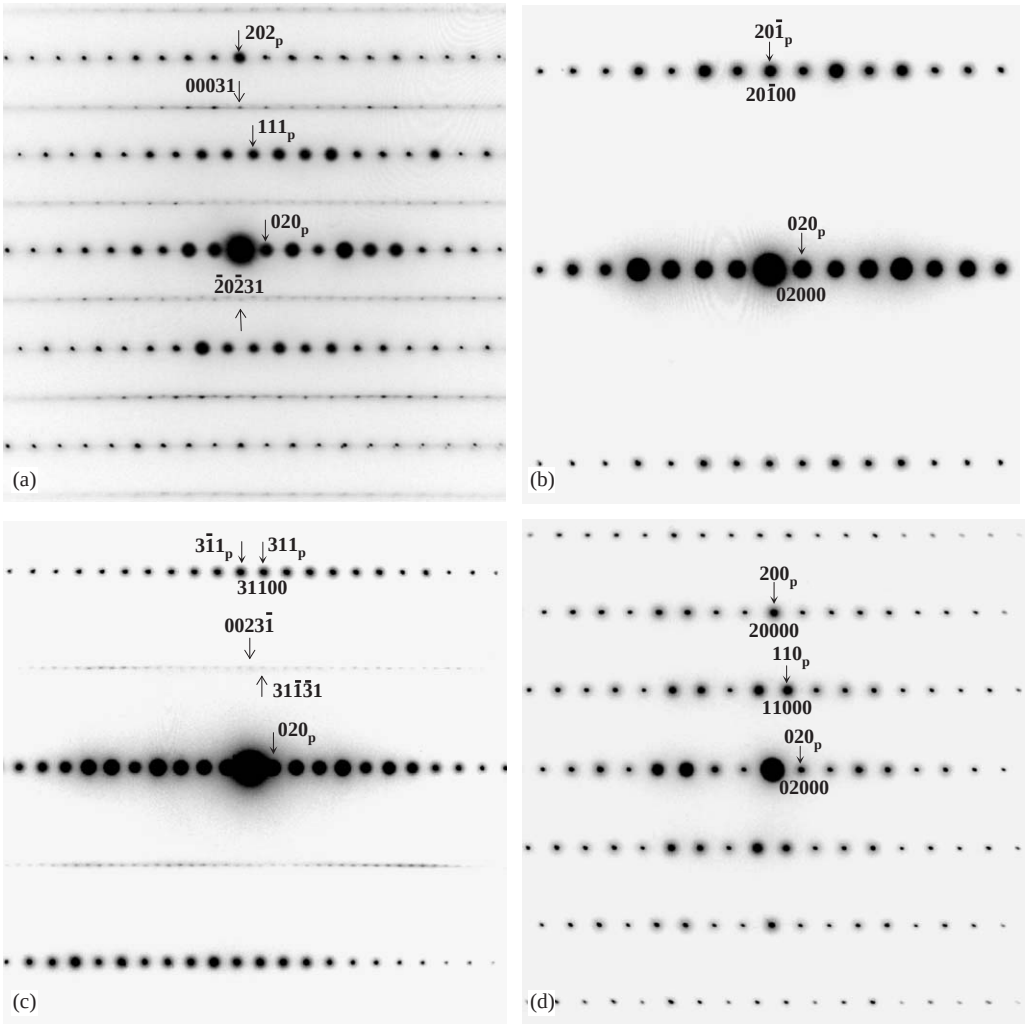

Fig. 4. Typical (a) $[\bar{1}01]_p$, (b) $[102]_p$, (c) $[\bar{1}03]_p$ and (d) $[001]_p$ zone axis EDPs of the $LaSb_2Sn_x$ compounds. (a) and (d) are from the $x = 0.5$ compound while (b) and (c) are from the $x = 0.6$ compound.

Reflections $HKL00$ thus correspond to $[HKL]^*$ parent Bragg reflections of the $LaSb_2$ sub-structure while reflections labelled $0K0MN$ correspond to $[MKN]^*$ parent Bragg reflections of the Sn sub-structure. Each component sub-structure then modulates the other with a periodicity determined by their mutual incommensurability along both **a*** and **c***. This interaction between the two parent sub-structures then induces a much weaker set of additional satellite reflections (such as, for example, those labelled $0\,0\,4\,1\,\bar{1}$ and $0\,0\,4\,\bar{1}\,\bar{1}$ in Fig. 5a). This explains the observed intensity asymmetry apparent in Figs. 5a and b.

The relative sharpness of the well-annealed Sn sub-structure parent reflections along both **a*** and **c*** (cf. Figs. 3a and b with Fig. 5b) and even **b***, although to a lesser extent (see Fig. 4), shows that the Sn sub-structure while not totally long-range ordered (as is apparent from the existence of diffuse streaking) is nonetheless rather well ordered, particularly in the Sn-containing (010) planes. The only observed systematic extinction conditions are as follows:

$$F(HKLMN) = 0 \text{ unless } H + K \text{ and } M + N \text{ are both even and}$$

$$F(H0LMN) = 0 \text{ unless } H \text{ and } L \text{ as well as } M + N \text{ are all even}$$

when indexed with respect to the $LaSb_2$ sub-structure, requiring the superspace centering operations $\{x_1 + \frac{1}{2},\ x_2 + \frac{1}{2},\ x_3,\ x_4,\ x_5\}$ and $\{x_1,\ x_2,\ x_3,\ x_4 + \frac{1}{2},\ x_5 + \frac{1}{2}\}$ as well as the *c*-hyperglide perpendicular to the **b** operation $\{x_1,\ -x_2,\ x_3 + \frac{1}{2},\ x_4,\ x_5\}$. The equivalent extinction conditions when indexed with respect to the Sn sub-structure are

$$F(HKLMN)\mathrm{Sn} = 0 \text{ unless } H + L \text{ and } K + M \text{ are both even and}$$

$$F(H0LMN)\mathrm{Sn} = 0 \text{ unless } M \text{ and } N \text{ as well as } H + L \text{ are all even}$$

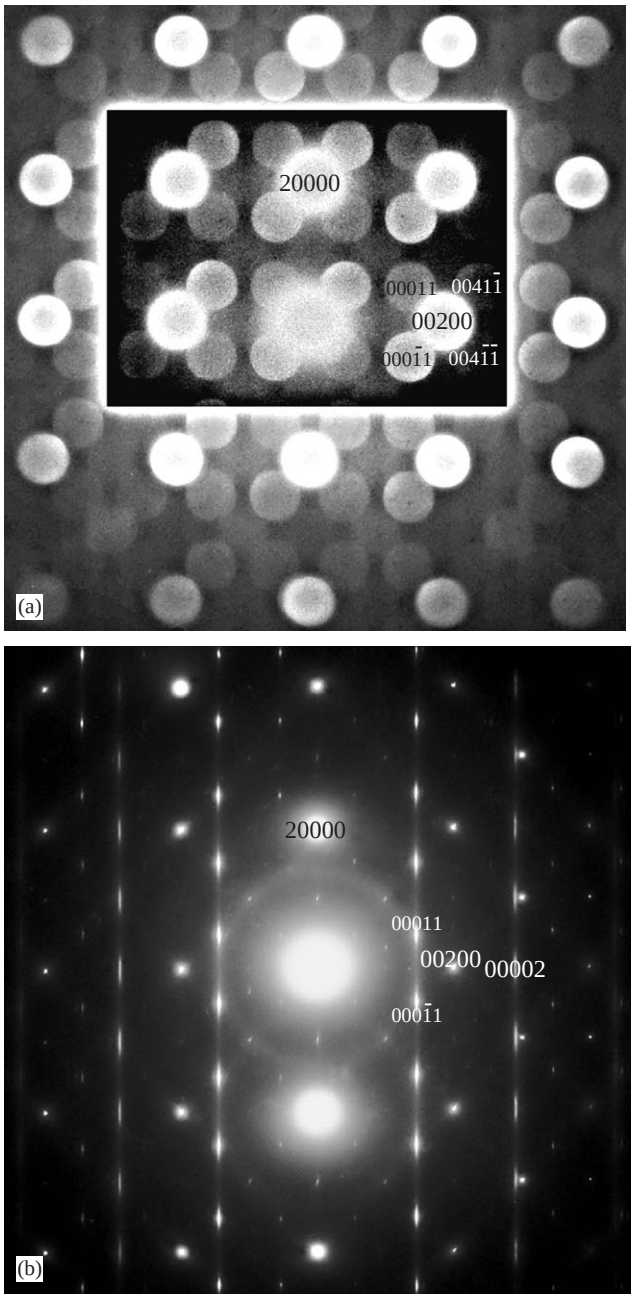

Fig. 5. (a) An $[010]_p$ convergent beam EDP. Note the disparity in relative intensities between the strongest satellite reflections immediately on either side of the 00200 parent $LaSb_2$ sub-structure reflection. The satellite reflections to the left (labelled 00011 and $000\bar{1}1$ in Fig. 5a) are significantly more intense than the equivalent satellite reflections to the right of 2110 (labelled $004\bar{1}1$ and $00\bar{4}\bar{1}\bar{1}$). (b) Close to $[010]_p$ EDP of the nominally $x = 0.3$ compound. Obtained by tilting a few degrees away from an exact $[010]_p$ zone axis orientation around a 200_p* systematic row.

requiring the superspace centering operations $\{x_1, x_2 + \frac{1}{2}, x_3, x_4 + \frac{1}{2}, x_5\}_{Sn}$ and $\{x_1 + \frac{1}{2}, x_2, x_3 + \frac{1}{2}, x_4, x_5\}_{Sn}$ as well as the hyperglide perpendicular to the **b** operation $\{x_1, -x_2, x_3, x_4, x_5 + \frac{1}{2}\}_{Sn}$ (using the above W matrix). The parent Sn sub-structure is thus necessarily B-centred

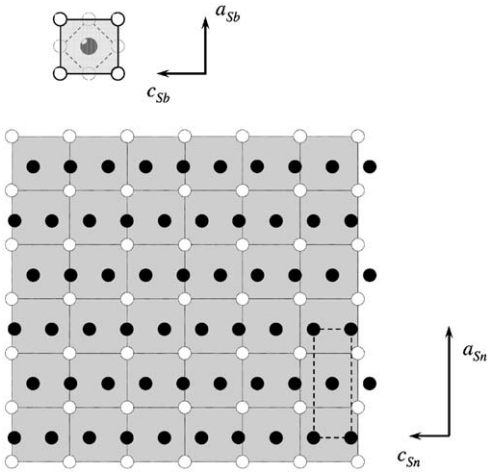

Fig. 6. The top part shows a single $LaSb_2$ square anti-prism with the Sb atoms white and the La atoms dark. The bottom part shows the top of an $LaSb_2$ bi-layer along with the (010) plane of Sn atoms immediately above it viewed in the *ac*-plane. The Sb(2) atoms are white while the Sn atoms are black in this part of the figure. The incommensurate relationship between the two sub-structures along the c direction is clearly visible. See text for details. For ease of illustration, a_{Sn} is here drawn as $2a_{LaSb2}$.

(see Fig. 6) and with a b-axis repeat $\frac{1}{2}$ that of the $LaSb_2$ sub-structure. There are thus 4 Sn atoms per Sn sub-structure unit cell at $\mathbf{r}_{Sn1} = 000$; $\mathbf{r}_{Sn2} = 0, \frac{1}{2}, 0$; $\mathbf{r}_{Sn3} = \frac{1}{2}, 0, \frac{1}{2}$; and $\mathbf{r}_{Sn4} = \frac{1}{2}, \frac{1}{2}, \frac{1}{2}$ respectively.

The implied overall superspace group symmetry [8,11,12] appears to be $Cmcm$ ($\mathbf{q}_1 = (\frac{1}{2} + \varepsilon_1)\mathbf{a}_p^*, \mathbf{q}_2 = (\frac{3}{2} - \varepsilon_1)\mathbf{c}_p^*$) or, possibly, a sub-group thereof. (The remaining generating operations of this superspace group, in addition to those given above, can be chosen to be $\{-x_1, x_2, x_3, -x_4, x_5\}$ and $\{-x_1, -x_2, -x_3, -x_4, -x_5\}$.) The observed streaking of the satellite reflections perpendicular to $\mathbf{c}_p$*, in particular, along the $\mathbf{b}_p$* direction of reciprocal space (see Fig. 4), shows that there is nonetheless some (considerable) disorder associated with this $(3+2)$-d composite modulated structure.

4. Discussion

The positions of the Sn atoms when refined with respect to the $Cmcm$, $LaSb_2$ sub-structure (see e.g. Figs. 1 and 2 of [1]) are apparently always in register along the a direction, modulated with a relatively small amplitude along the b direction but liquid-like along the c direction with closely spaced, partially occupied, split atom positions being reported [1,2]. Given that the Sn and $LaSb_2$ sub-structures are, in general, mutually incommensurable along both the a and c directions (see Fig. 3), this implies quite a different type of behaviour for the Sn atom displacive Atomic Modulation Functions (AMFs) [8,11–15] along these directions. Such displacive AMF components describe the deviation in position of

the Sn atoms (along the a and c directions) away from their average sub-structure positions ($\mathbf{r}_{Sn}+\mathbf{t}_{Sn}$; $\mathbf{r}_{Sn}$ the position within the Sn sub-structure unit cell and $\mathbf{t}_{Sn}$ a lattice vector of the Sn sub-structure) as a function of $\bar{x}_4 = \mathbf{a}^*_{LaSb2} \cdot [\mathbf{r}_{Sn} + \mathbf{t}_{Sn}]$ and $\bar{x}_5 = \mathbf{c}^*_{LaSb2} \cdot [\mathbf{r}_{Sn} + \mathbf{t}_{Sn}]$—see e.g. [14,15]).

For the Sn sub-structure to always stay in register with the $LaSb_2$ sub-structure along the a direction (located mid-way between neighbouring c-axis columns of Sb atoms in projection along **b**—see Fig. 6) independently of its location along the c direction as it apparently does (see [1,2]), despite the fact that the Sn and $LaSb_2$ sub-structures are in general mutually incommensurable with $a_{Sn} = \{1/(\frac{1}{2}+\varepsilon_1)\}a_{LaSb2} = (2-\delta_1)a_{LaSb2}$), the Sn1 displacive AMF along the a direction as a function of $\bar{x}_4$ must necessarily take the saw-tooth form shown in Fig. 7b (the solid line) and be independent of $\bar{x}_5$. Note that the Sn sub-structure superspace symmetry operation $\{x_1, x_2+\frac{1}{2}, x_3, x_4+\frac{1}{2}, x_5\}_{Sn}$ constrains the corresponding Sn2 displacive AMF along the a direction as a function of $\bar{x}_4$ to take the form represented by the dashed line in Fig. 7b i.e. $\mathbf{u}_{Sn2,x}(\bar{x}_4+\frac{1}{2}, \bar{x}_5) = \mathbf{u}_{Sn1,x}(\bar{x}_4, \bar{x}_5)$, as shown in Fig. 7b. Thus Sn1 and Sn2 atoms initially directly above one another in the average Sn sub-structure (see Fig. 7a) always tend to move in opposite directions in the resultant modulated structure (see the arrows in Fig. 7c) in such a way as to maintain registry with the $LaSb_2$ sub-structure along the a direction (represented by the vertical dashes in Fig. 7c).

For the purposes of illustrating more concretely the corresponding real space effect on the relative positioning of the Sn1 and Sn2 atoms along the a direction, the parameter δ_1 has been taken as $\frac{1}{10}$ in Fig. 7 so that $\bar{x}_4(Sn1) = \mathbf{a}^*_{LaSb2}.[\mathbf{r}_{Sn1}+\mathbf{t}_{Sn}] = (2-\frac{1}{10})\mathbf{a}^*_{Sn}.[n\mathbf{a}_{Sn}] = (2-\frac{1}{2})n$. The ($n = 1, 2, \ldots$ to 10) Sn1 atoms per resultant supercell are then represented by the open circles with the label n in Figs. 7b and c while the corresponding ($n' = 1, 2, \ldots$ to 10) Sn2 atoms initially directly above the Sn1 atoms (see Fig. 7a) are represented by the closed circles with the label n'. Starting at the $n = 0$ Sn1 atom, such a displacive AMF implies that the average Sn–Sn separation distance along a_{Sn} initially expands slightly (shown by the horizontal arrows in Fig. 7c) to $2a_{LaSb2}$ to keep in register with the $LaSb_2$ sub-structure repeat (represented

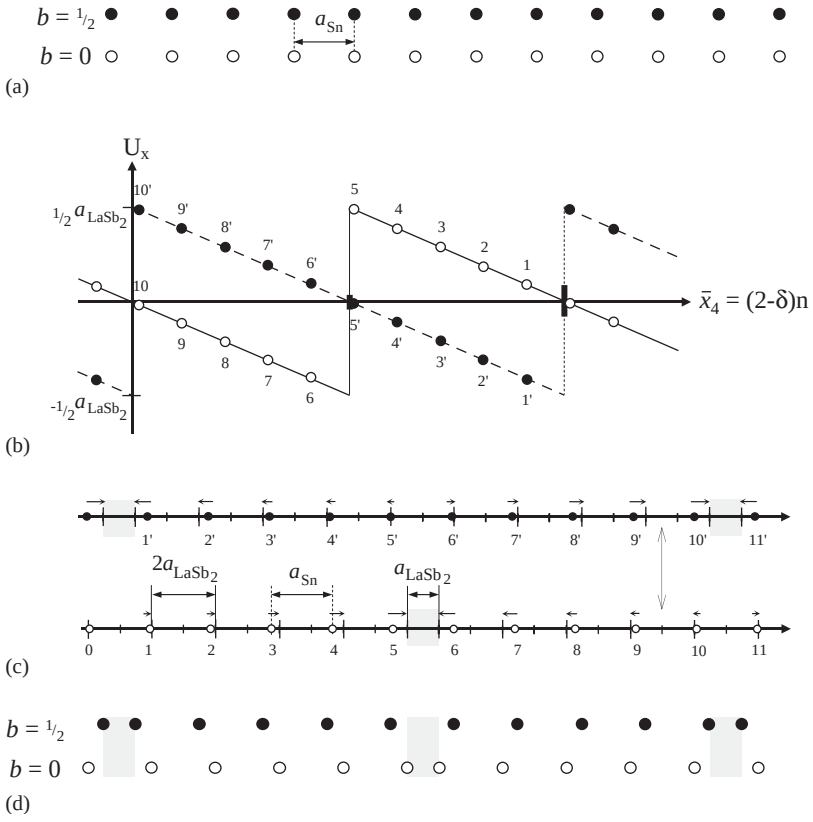

Fig. 7. The saw-tooth shaped Sn displacive AMF (along the a direction) required if the Sn atom is to stay in register with the underlying $LaSb_2$ sub-structure along the a direction. The average Sn sub-structure repeat of slightly less than $2a_{LaSb2}$ can be achieved via the regular introduction of anti-phase boundaries at intervals along a_{Sn} which depend upon the magnitude of the parameter δ_1. (i) Shows two columns of Sn atoms viewed along the crystallographic c axis. The open circles represent a string of Sn1 atoms at $y = 0$ while the filled circles represent a similar string of Sn2 atoms at $y = \frac{1}{2}$. See text for details.

by the vertical dashes in Fig. 7c) until atom $n = 6$ at which stage it contracts discontinuously to a local $1a_{LaSb2}$ separation distance prior to exanding again to a $2a_{LaSb2}$ separation distance.

Figs. 7c and d show that the 'average' Sn sub-structure repeat of slightly less than $2a_{LaSb2}$ (see e.g. Fig. 3a) can then be achieved via the regular introduction of anti-phase boundaries at intervals along a_{Sn} which depend upon the magnitude of the parameter δ_1 (as shown for the $y = \frac{1}{2}$ Sn layer perpendicular to **b** in Fig. 8). Note that any irregularity in the spacing of these anti-phase boundaries along $\mathbf{a}_{Sn}$ would have the effect of rapidly diminishing the intensity of high h_{Sn} sub-structure Bragg reflections that one might expect given a well-ordered saw-tooth displacive AMF. Too much irregularity would also lead to smearing of the Sn sub-structure Bragg reflections along **a***, just as is observed experimentally particularly for the 48 h annealed specimens (see e.g. Fig. 5b). As noted above, the superspace centering operation $\{x_1,\ x_2 + \frac{1}{2},\ x_3,\ x_4 + \frac{1}{2},\ x_5\}_{Sn}$ links the *a*-axis displacive AMF of the Sn2 atoms initially separated by $\frac{1}{2}\mathbf{b}_{LaSb2}$ in such a way that these Sn atoms always move in a direction opposite to that of the Sn1 atoms. The resultant positioning of the anti-phase boundaries perpendicular to $\mathbf{a}_{Sn}$ at the $y = \frac{1}{2}$ level thus occur mid-way between the anti-phase boundaries at the $y = 0$ level (see Figs. 7d and 8). The result is entirely compatible with Fig. 1 of [1] (Fig. 9).

Along the *c* direction, the fact that the Sn atoms give rise to a virtually continuous streak when the true Sn sub-structure is folded back into the $LaSb_2$ sub-structure cell [1,2] suggests that the displacive AMF of the Sn atoms along *c* as a function of $\bar{x}_4$ and $\bar{x}_5$ must be of relatively small amplitude. We would then expect the Sn atoms to give rise to a virtually continuous streak along **c** (see e.g. [8,11–15]; see also Fig. 6), indeed this is one of the characteristics of any composite modulated structure. The reported split Sn positions are simply attempting to mimic what is really going on. It is worth pointing out that one of the copper atoms in the refined average structure/s of the ACu_7S_4 ($A = NH_4$, K, Tl and Rb) family of compounds behaves in a very similar 1-*d* liquid-like manner [16].

Matters, however, are not quite as simple as just described. Consider, in particular, the apparently composition-independent relation $c^*_{Sn} \sim (\frac{3}{2} - \delta_2)c^*_{LaSb2}$ (see Fig. 3). This requires that $c_{Sn} \sim (\frac{2}{3})c_{LaSb2}$ for any Sn

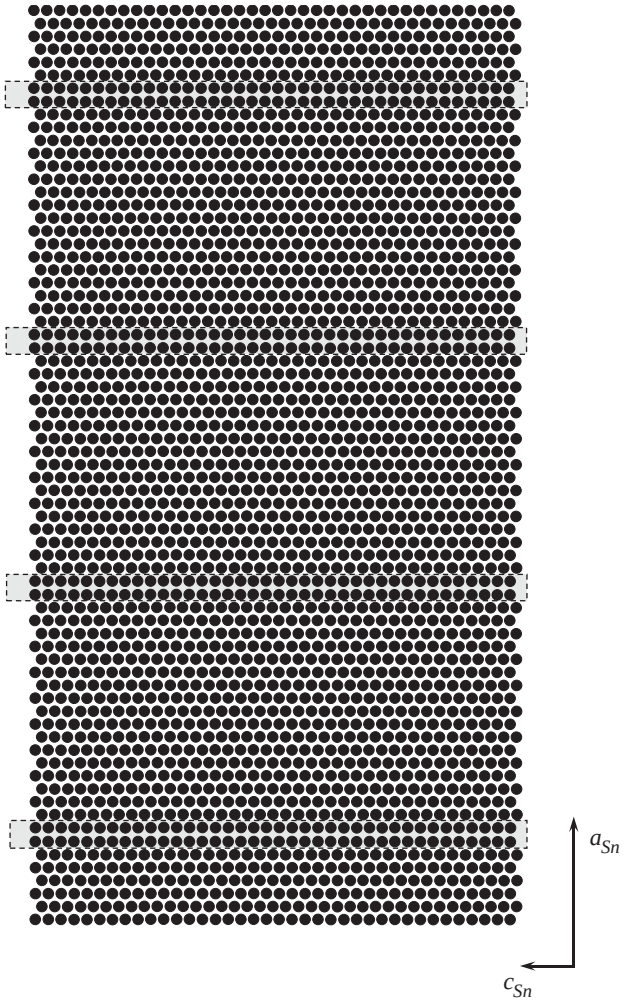

Fig. 8. Shows the distribution of Sn atoms at the $y = \frac{1}{2}$ level implied by the saw-tooth AMFs shown in Fig. 7. The regular introduction of anti-phase boundaries at regular intervals along a_{Sn} (dependent upon the magnitude of the parameter δ_1) gives rise to an average Sn sub-structure repeat of slightly less than $2a_{LaSb2}$.

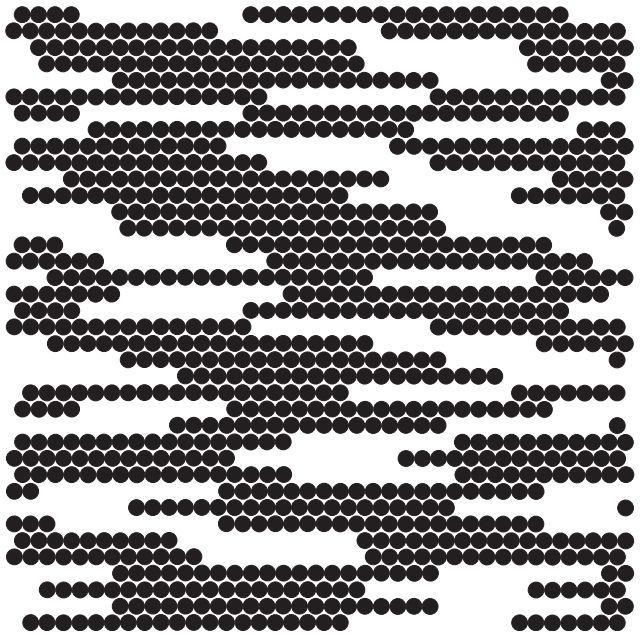

Fig. 9. Schematic representation of the tin atom ordering of $LaSb_2Sn_x$ in one particular *ac*-plane. The length of the strings of Sn atoms in relation to the length of the vacancies is set by the composition of the compound. Here the ordering rule is that 20 Sn atoms are always followed by 10 vacancies (giving $LaSb_2Sn_{0.5}$). The starting point for any one such string along *c* is random.

content (see Fig. 6). This is not what one expects for a 'normal' composite modulated structure. Why might this be so? Given that there are two $(LaSb_2)_2$ bi-layer units and two Sn strings per $LaSb_2$ sub-structure unit cell (see Fig. 1a), the 'average' Sn–Sn separation distance along each of the [001] strings must be given by $c_{Sn} = (\frac{1}{2x})c_{LaSb2}$ for composition $LaSb_2Sn_x$. For the end-member composition $x = 0.75$, this corresponds to an average Sn–Sn separation distance of $(\frac{2}{3})c_{LaSb2}$ or ~3.004 Å using the reported c_{LaSb2} sub-cell dimension. Intriguingly, the distance of closest approach of Sn atoms in the most common β, or metallic, form of elemental Sn is virtually identical to this value at 3.022 Å. This points towards a metal-like Sn sub-structure and would explain why the tin content can vary so much without any apparent changes in the oxidation states for La and Sb. It is also consistent with the fact that the isomer shifts for the Sn atoms observed by ^{119}Sn Mössbauer spectroscopy in $LaSb_2Sn_x$ are essentially identical to those of elemental β-Sn [2].

The fact that c_{Sn}* continues to obey the relation $(c^*_{Sn} \sim \frac{3}{2}c^*_{LaSb2})$ apparently regardless of the value of x (see e.g. Figs. 3a and b) shows experimentally that the removal of Sn atoms from the [001] strings does not occur homogeneously (i.e. through the expansion of the local Sn–Sn separation distance) but rather through the segmentation of the initially (for $x = 0.75$) infinite metallic Sn chains along $\mathbf{c}_{Sn}$ into finite units as first proposed in [2] (see e.g. Figs. 8 and 3 of [2]). These one-dimensional Sn chains must still be of considerable length, however, otherwise the Sn sub-structure reflections would be streaked out not only perpendicular to **c*** but also along **c***. Experimentally, this is not noticeably the case (see e.g. Figs. 3–5). The fact that the Sn sub-structure parent reflections are still quite sharp not only along **c*** but also along **a*** and even **b*** shows that these [001] strings are quite well ordered not only along [001] but also from string to string. It is worth pointing out that Sn atom ordering of the type shown in Fig. 8 would automatically give rise to diffuse streaking along a_p* just as is observed experimentally (cf., for example, Figs. 3a and b with Plate 18 of [17].

Along the b direction, the average structure refinements of [1,2] suggest that there also exists a relatively small amplitude (~0.0089×23.1 ~0.21 Å—see Table 2 of [1]), probably sinusoidal modulation of the positions of the Sn atoms along b dependent upon $\bar{x}_5$ i.e. upon the relative positioning of the Sn sub-structure with respect to the $LaSb_2$ sub-structure along the c direction (see e.g. Fig. 6). It is difficult, however, to go further without a full $(3+2)$-d incommensurate structure refinement. Unfortunately, the apparently unavoidable streaking/disorder associated with the Sn sub-structure may make such a $(3+2)$-d incommensurate structure refinement very difficult if not impossible.

References

[1] M.J. Ferguson, R.W. Hushagen, A. Mar, Inorg. Chem. 35 (1996) 4505–4512.
[2] L. Deakin, M.J. Ferguson, M.J. Sprague, A. Mar, R.D. Shama, C.H.W. Jones, J. Solid State Chem. 164 (2002) 292–300.
[3] A.M. Mills, R. Lam, M.J. Ferguson, L. Deakin, A. Mar, Coord. Chem Rev. 233–234 (2002) 207–222.
[4] G. Papoian, R. Hoffmann, J. Am. Chem. Soc. 123 (2001) 6600–6608.
[5] R. Wang, H. Steinfink, Inorg. Chem. 6 (9) (1967) 1685–1692.
[6] J. Schoenes, W. Basca, F. Hulliger, Solid State Commun. 88 (1988) 287.
[7] R.L. Withers, R. Vincent, J. Schoenes, J. Solid State Chem. 177 (2004) 701–708.
[8] R.L. Withers, S. Schmid, J.G. Thompson, Prog. Solid State Chem. 26 (1998) 1–96.
[9] F.J. Brink, L. Norén, R.L. Withers, J. Solid State Chem. 177 (2004) 2177–2182.
[10] B. Noläng, Inst. Materialkemi, Ångströmlaboratoriet, Box 538, S-751 21 Uppsala, Sweden.
[11] S. van Smaalen, Cryst. Rev. 4 (1995) 79–202.
[12] M. Carter, R.L. Withers, Z. Kristallogr. 219 (2004) 763–767.
[13] J.M. Pérez-Mato, G. Madariaga, F.J. Zuniga, A. Garcia Arribas, Acta Crystallogr. A 43 (1987) 216–226.
[14] Ph. Boullay, G. Trolliard, D. Mercurio, J.M. Perez-Mato, L. Elcoro, J. Solid State Chem. 164 (2002) 252–260.
[15] Ph. Boullay, G. Trolliard, D. Mercurio, J.M. Perez-Mato, L. Elcoro, J. Solid State Chem. 164 (2002) 261–271.
[16] L. Norén, K. Larsson, R.G. Delaplane, R. Berger, J. Alloy Compd. 314 (2001) 114–123.
[17] G. Harburn, C. Taylor, T.R. Welberry, Atlas of Optical Transforms, Plate 18, The Open University ST291, Bell and Hyman Ltd., 1988.